Systems/Circuits

Activity Patterns Elicited by Airflow in the Olfactory Bulb and Their Possible Functions

Ruiqi Wu,[1] Yue Liu,[2] Li Wang,[1] Bo Li,[1] and Fuqiang Xu[1,2]

[1]State Key Laboratory of Magnetic Resonance and Atomic and Molecular Physics, Key Laboratory of Magnetic Resonance in Biological System, Wuhan Institute of Physics and Mathematics, Center of Excellence for Brain Science and Intelligent Technology, the Chinese Academy of Sciences, Wuhan 430071, China, and [2]Wuhan National Laboratory for Optoelectronics, Wuhan 430074, China

Olfactory sensory neurons (OSNs) can sense both odorants and airflows. In the olfactory bulb (OB), the coding of odor information has been well studied, but the coding of mechanical stimulation is rarely investigated. Unlike odor-sensing functions of OSNs, the airflow-sensing functions of OSNs are also largely unknown. Here, the activity patterns elicited by mechanical airflow in male rat OBs were mapped using fMRI and correlated with local field potential recordings. In an attempt to reveal possible functions of airflow sensing, the relationship between airflow patterns and physiological parameters was also examined. We found the following: (1) the activity pattern in the OB evoked by airflow in the nasal cavity was more broadly distributed than patterns evoked by odors; (2) the pattern intensity increases with total airflow, while the pattern topography with total airflow remains almost unchanged; and (3) the heart rate, spontaneous respiratory rate, and electroencephalograph power in the β band decreased with regular mechanical airflow in the nasal cavity. The mapping results provide evidence that the signals elicited by mechanical airflow in OSNs are transmitted to the OB, and that the OB has the potential to code and process mechanical information. Our functional data indicate that airflow rhythm in the olfactory system can regulate the physiological and brain states, providing an explanation for the effects of breath control in meditation, yoga, and Taoism practices.

Key words: airflow map; airflow rhythm; functional MRI; mechanosensitivity; olfactory bulb

Significance Statement

Presentation of odor information in the olfactory bulb has been well studied, but studies about breathing features are rare. Here, using blood oxygen level-dependent functional MRI for the first time in such an investigation, we explored the global activity patterns in the rat olfactory bulb elicited by airflow in the nasal cavity. We found that the activity pattern elicited by airflow is broadly distributed, with increasing pattern intensity and similar topography under increasing total airflow. Further, heart rate, spontaneous respiratory rate in the lung, and electroencephalograph power in the β band decreased with regular airflow in the nasal cavity. Our study provides further understanding of the airflow map in the olfactory bulb *in vivo*, and evidence for the possible mechanosensitivity functions of olfactory sensory neurons.

Introduction

The best-known functions of the olfactory system are odor detection, discrimination, and identification, which are important for animal survival because they are involved in feeding, foraging, mating, communicating, and avoiding predators (Shipley and Ennis, 1996; Firestein, 2001). The diverse olfactory perceptions rely on ~1000 types of odorant receptors (ORs) expressed by olfactory sensory neurons (OSNs) located in the olfactory epithelium (OE; Buck and Axel, 1991). Odor information is transduced by the OSNs, processed in the olfactory bulb (OB), and then sent to the olfactory cortices (Lledo et al., 2005). The OB is the hub for olfactory information coding and processing in the olfactory system. To date, it is generally accepted that the information of a

Received Aug. 4, 2017; revised Sept. 23, 2017; accepted Sept. 28, 2017.

Author contributions: R.W., B.L., and F.X. designed research; R.W. and L.W. performed research; R.W. and Y.L. analyzed data; R.W. and F.X. wrote the paper.

This work is supported by the National Basic Research Program (973 Program) of China (Grant No. 2015CB755601 to F.X.), the National Natural Science Foundation of China (Grants No. 81661148053 and No. 91632303 to F.X.), and the Strategic Priority Research Program of Chinese Academy of Sciences (Grant No. XDB02050005 to F.X.). We thank Tung-Lin Wu for language editing of the manuscript.

The authors declare no competing financial interests.

Correspondence should be addressed to either of the following: Fuqiang Xu, PhD, Professor, Wuhan Institute of Physics and Mathematics, the State Key Laboratory of Magnetic Resonance and Atomic and Molecular Physics, the Chinese Academy of Sciences, Wuhan 430071, China. E-mail: fuqiang.xu@wipm.ac.cn; or Ruiqi Wu, PhD, Wuhan Institute of Physics and Mathematics, the State Key Laboratory of Magnetic Resonance and Atomic and Molecular Physics, the Chinese Academy of Sciences, Wuhan 430071, China. E-mail: wuruiqiqi@126.com.

DOI:10.1523/JNEUROSCI.2210-17.2017

 0270-6474/17/3710700-12$15.00/0

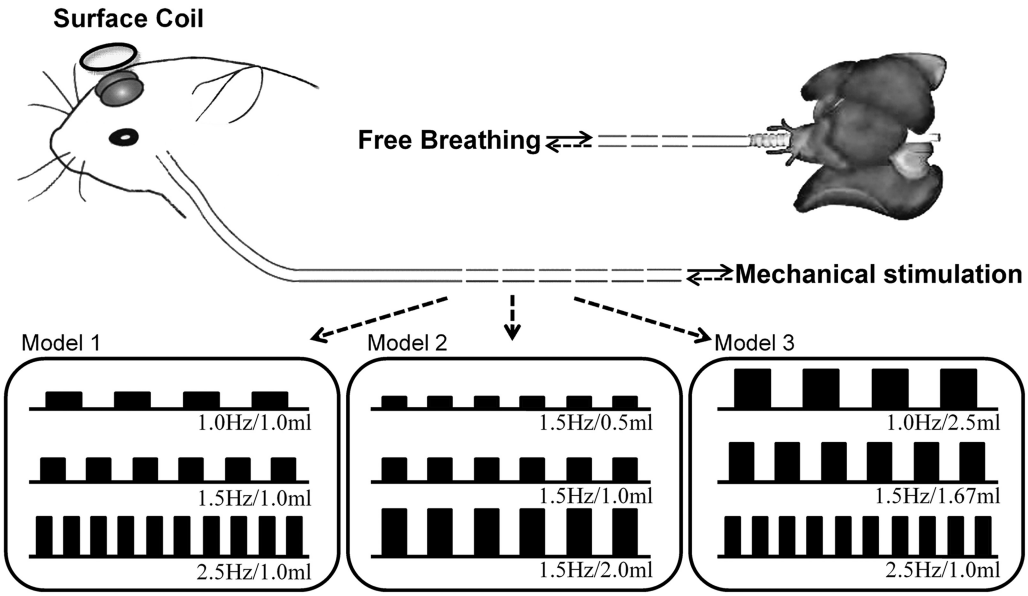

Figure 1. Diagram of the mechanical stimulus models. The tube connected to the opened trachea for transporting pure air to the nasal cavity was linked to a ventilator, which controls the flow rate of the mechanical stimulation. Another tube connected to the lungs was kept opened for free breathing. Three stimulus models were used: Model I: fixed tidal volume with varying frequency (1.0 Hz/1.0 ml, 1.5 Hz/1.0 ml, and 2.5 Hz/1.0 ml); Model II, fixed frequency and varying tidal volume (1.5 Hz/0.5 ml, 1.5 Hz/1.0 ml, and 1.5 Hz/2.0 ml); and Model III, fixed total airflow strength while tidal volume and frequency were varied simultaneously (1.0 Hz/2.5 ml, 1.5 Hz/1.67 ml, and 2.5 Hz/1.0 ml). Each model included three stimulation conditions, and a total of seven conditions were used (1.0 Hz/1.0 ml, 1.5 Hz/1.0 ml, 2.5 Hz/1.0 ml, 1.5 Hz/0.5 ml, 1.5 Hz/2.0 ml, 1.0 Hz/2.5 ml, and 1.5 Hz/1.67 ml).

given olfactory stimulus is encoded by a specific spatiotemporal activity pattern in the OB (Xu et al., 2000a; Wachowiak and Shipley, 2006). Previous studies have shown that rhythmic activity of the OB is coupled with respiration, suggesting that the OSNs can sense airflow information (Ueki and Domino, 1961; Macrides and Chorover, 1972; Onoda and Mori, 1980; Fontanini et al., 2003; Phillips et al., 2012). *In vitro* data have revealed that many OSNs are indeed capable of sensing mechanical stimulation (Grosmaitre et al., 2007), which means OSNs may play roles for detecting both odors and airflow. For both odors and airflow, this detection is probably mediated by the same cAMP cascade. Recently, a study reported that OSNs expressing different olfactory receptor types display different responses to mechanical stimuli, suggesting that G-protein-coupled receptors may have an overlooked role as mechanosensors, and adding to the growing list of polymodal transmembrane receptors in sensory organs (Connelly et al., 2015). However, how the information of mechanical airflow is represented globally in the OB *in vivo* has not been revealed yet, despite the indicated importance of mechanical sensing in the olfactory system to brain functions.

Blood oxygen level-dependent functional MRI (BOLD-fMRI) has the advantages of noninvasiveness, high penetrability, and decent spatial and temporal resolutions, making it an essential tool for *in vivo* functional studies containing large sampling volumes. Thus, it has been widely used in the field of neuroscience for the past 20 years (Logothetis, 2008; Bandettini, 2012). In the olfactory system, it has been successfully used to map the activity patterns evoked by odorants in rodent OBs (Xu et al., 2005; Schafer et al., 2006; Martin et al., 2007; Li et al., 2014; Poplawsky and Kim, 2014; Poplawsky et al., 2015; Murphy et al., 2016; Sanganahalli et al., 2016) and even in nonhuman primates (Zhao et al., 2015).

By using BOLD-fMRI and local field potentials (LFPs), we investigated the activity patterns elicited by different airflow paradigms in the rat OB, and the effects of these paradigms on OB and physiological states of the animals. We observed an unspecific and stable mechanical map in the OB, and the pattern intensity significantly depended on the stimulating paradigms. Also, heart rate, spontaneous respiratory rate, and electroencephalograph (EEG) power in the β band were reduced under regular airflow stimulation. Our study provides knowledge of the mechanical map and sensation profiles in the OB *in vivo*, and the possible functions of mechanical perception in the olfactory system.

Materials and Methods

Animal preparation and stimulation. Adult male Sprague Dawley rats (250–350 g) were preanesthetized with 2.5% isoflurane as reported previously (Wachowiak and Cohen, 2001). Endotracheal intubation was subsequently performed on 19 animals (i.e., six animals were used for MRI study, five animals were used for electrophysiology experiment, and eight animals were used for physiology signal acquisitions) and the tube connected to the lungs was kept opened for free breathing. The tube inserted to the anterior end of the dissected trachea (pharynx side) was connected to a medical ventilator (HX-100E, TME) to generate artificial respiration paradigms. The airflow in the nasal cavity was controlled by a ventilator within the physiological ranges: airflow tidal volume, 0.5–2.0 ml; airflow frequency, 1–2.5 Hz (Fig. 1). The choice of airflow parameters was based on the regular breathing range of rats reported in previous studies (Pass and Freeth, 1993; Strohl et al., 1997; Legaspi et al., 2010) and indicated in this study (see Fig. 7*B*). Three stimulation models were designed. Specifically, Model I tidal volume was fixed and the frequency was varied (1.0 Hz/1.0 ml, 1.5 Hz/1.0 ml, and 2.5 Hz/1.0 ml); Model II frequency was fixed and the tidal volume was varied (1.5 Hz/0.5 ml, 1.5 Hz/1.0 ml, and 1.5 Hz/2.0 ml); and Model III tidal volume and frequency were varied simultaneously but the total airflow rate was fixed (1.0 Hz/2.5 ml, 1.5 Hz/1.67 ml, and 2.5 Hz/1.0 ml). The pressures of the airflow (P) were estimated by using the following physical equation: $P = 0.5 \times \rho \times v^2$, where ρ is the air density (1.2 kg/m^3) and v is the air velocity. Here, v is determined by the stimulation parameters. Within a given period of time (t), the total air volume (V) can be calculated by the mathematical formula of $V = tv \times f \times t$, where tv is the tidal volume, and f is the stimulation frequency. Also, the total air volume flowed through the tube, equal to V, can be computed by the formula $V = 1/4 \times \pi \times d^2 \times v \times t \times dr$, where d is the inner diameter (1.6 mm) of the tube inserted to the anterior end of the dissected trachea, and dr is the duty

ratio of the stimulation (50%). Since the stimulation scope performed in this study was from 1.5 Hz/0.5 ml to 1.5 Hz/2 ml, the air velocity was estimated as from 0.75 to 2.99 m/s. Therefore, the pressures of airflow were from 0.34 to 5.36 Pa. The air was purified by charcoal filtration before being delivered into the ventilator. During "on-stage" of retronasal stimulation, the anterior-nasal flow was able to reach a piece of small paper placed in front of the rat's nose. This was performed to ensure the presentation of air successfully reached the nasal epithelia. The term "airflow" used throughout this paper, such as "airflow stimulation" and "airflow map," represents nasal airflow caused by artificial ventilation.

Additionally, five free-breathing rats were used for odor map study. Either 5% amyl acetate or hexanal (Sigma-Aldrich) was delivered into the nasal cavity, as shown in our previous works (Xu et al., 2005; Li et al., 2014). The odorants were dissolved in paraffin oil to dilute the concentration to 5%, which could elicit a robust response in the OB (Xu et al., 2005; Li et al., 2014). The odor stimulation period was synchronized with the data acquisition by a solenoid valve, which was driven by a digital to analog converter. Air (off) or odorized air (on) was delivered to the nose at a constant rate of 1 l/min to eliminate the effect of the airflow.

The skin on top of the OB was removed to expose the skull before MRI acquisitions. After surgery was performed, the anesthetic was switched to urethane (1.5 k/kg, i.p.). All animal procedures were approved by the Chinese Academy of Sciences. All animals were housed under specific pathogen-free conditions at the Wuhan Institute of Physics and Mathematics, as approved by the Chinese Academy of Sciences.

BOLD-fMRI data acquisition. MRI experiments were performed on a horizontal-bore 7.0 tesla BioSpec MRI instrument (Bruker). The procedures for animal preparation are referenced in our previous reports (Xu et al., 2003, 2005; Li et al., 2014). Briefly, the animal's head was fixed in a holder to minimize movement, and the animal was laid on a water heating bed to maintain normal body temperature at ~37°C. The respiration rate of the animal was monitored by a piezoelectric device. A circular transmitting and receiving surface coil (10 mm diameter) was placed above the animal's OB to maximize signal-to-noise ratio (SNR). fMRI data were acquired in coronal slices of the OB using a multisegment gradient echo planar sequence (segment number, 2; TR = 2000 ms; TE = 14 ms; flip angle, 45–60°; FOV, 16 × 16 mm; slice number, 6; spatial resolution, 0.2 × 0.2 × 0.5 mm). The stimulation block was performed using 32 s (eight frames) before stimulation as baseline, 16 s (four frames) during stimulation as activation, and 80 s (20 frames) after stimulation as recovery. The stimulation was synchronously controlled by the data acquisition system. Four trials were performed for each stimulus paradigm (two odor and seven mechanical conditions) on all animals, with a ~10 min interstimulation interval to minimize habituation. The animals were randomized to an ordering of the stimulus during the data acquisition. Five rats received stimuli of all three mechanical models, and one rat received only Model III stimuli. RARE (rapid acquisition with refocused echoes) T2-weighted anatomical images were obtained for the same slices as the functional images (TR = 3000 ms; effective TE = 80 ms; RARE factor, 4; average number, 15; total duration, ~30 min; spatial resolution, 0.1 × 0.1 × 0.5 mm).

LFP recording and physiology condition monitoring. LFP electrophysiology recording, which reflects neural activity directly, was used to verify the revealed results from fMRI. Physiological signals were quantified to analyze the alteration of physiological state induced by mechanical information.

Rats were placed on a stereotaxic holder (Stoelting) inside a Faraday cage on a vibration-free table. The skull above the OB (2 mm lateral to midline, 8 mm anterior to bregma) was carefully exposed, and holes with similar positions were drilled in each OB and then covered with mineral oil to prevent drying. Two uniform tungsten microelectrodes (~100 μm; A-M Systems) were inserted into the glomerular layer of bilateral OBs by using a stereotaxic micromanipulator (Stoelting). The skin of the neck was hooked with a silver wire as the reference signal. Each animal's body temperature was maintained at ~37°C, and respiratory rate was monitored by a pressure-sensitive device. The LFP signals were amplified (×2000; PGA32, Multichannel systems) before digitization (μ-1401, Cambridge Electronic Design). The mechanical stimulation block for LFP recording was the same as the ones used for fMRI experiments. All five animals included in the LFP experiment underwent the three stimulus paradigms (i.e., Model I: 1.0 Hz/1.0 ml, 1.5 Hz/1.0 ml, and 2.5 Hz/1.0 ml; Model II: 1.5 Hz/0.5 ml, 1.5 Hz/1.0 ml, and 1.5 Hz/2.0 ml; and Model III: 1.0 Hz/2.5 ml, 1.5 Hz/1.67 ml, and 2.5 Hz/1.0 ml).

Additionally, eight rats were used for respiratory rate, EEG, and electrocardiograph (ECG) acquisitions. A piezoelectric stretch sensor was placed under each animal's chest for autonomous respiration rate monitoring by detecting chest movement. The piezoelectric signal was subsequently amplified before digitization for respiratory signal recording. Two electrodes (diameter, ~100 μm) were placed subcutaneously into the left forepaw and the right hindpaw for ECG recording. The skull was exposed and epidural screw electrodes over the parietal cortex (4 mm lateral to midline, −2 mm anterior to bregma) and cerebellum (reference electrode) were implanted for EEG recordings. Physiology signals were amplified before digitization. Mechanical stimulation was set at 1.0 Hz/2.5 ml, and the stimulation block was performed as follows: 60 s before stimulation as baseline, 30 s during stimulation as activation, and 80 s after stimulation as recovery. Five to six trials were performed on each animal, with a ~10 min interstimulation interval to minimize habituation.

Experimental design and statistical analysis. All fMRI and LFP data were analyzed with Matlab (MathWorks, RRID:SCR_001622). Statistical analyses were performed by SPSS (IBM, RRID:SCR_002865). For each stimulus—mechanical Model I, mechanical Model II, and odor—20 trials involving five animals took place. For mechanical model III, 24 trials involving six animals took place. A total of 40 LFP trials from five animals (10 OBs) for each mechanical model, and 45 physiology trials from eight animals were included. Student's *t* test and ANOVA tests were used to evaluate the difference between two-group or multigroup signals. A p value of <0.05 was considered statistically significant. Results were represented as mean ± SE.

fMRI data analysis. All raw fMRI data were first preprocessed using SPM8 (University College London, RRID:SCR_007037). Realignment was performed to eliminate head movements and image shifts, and Gaussian smoothing was applied to improve the SNR (Gaussian low-pass filter, 3 × 3; σ, 0.8). For all experimental conditions in this report, motion artifacts were relatively minor (i.e., head rotation, $<0.2°$, head translation, $<1/5$ voxel size). The signal differences between baseline and stimulation periods were compared voxel by voxel to obtain Student's *t* values as indicators for activation. The individual slice activation was subsequently presented, by overlapping the *t* values from the four trials under the same stimulating condition in the same animal onto anatomical images, similar to what we have reported previously (Xu et al., 2003, 2005; Li et al., 2014). Time courses of BOLD signals in the OB were extracted. Slices of functional images were masked based on the OB edge as the region of interest (ROI). Time courses of signal changes ($\Delta S/S$) were generated from averaged signals of all voxels in the ROI. The eight frames before stimulation and four frames (frames 9–12) during stimulation were used as baseline and activation periods respectively. The signal changes during the stimulation stage were averaged as response intensities, which were averaged across trials for statistical analysis. Comparison was then performed between responses from different stimulus paradigms.

Map similarity analysis. To quantify the relationship between different maps (two odor maps and seven mechanical maps), three analyses were performed: activation rate, spatial correlation coefficient (SCC), and 2-D correlation. All stimulus-evoked activation maps were first thresholded ($t > 1.5$) before similarity calculations. Considering the distortion and variation in the first and last slice (slices 1 and 6), only the intermediary slices (slices 2–5) were analyzed for similarity.

We calculated the activation rate by dividing the voxel number in the activation area by the total number of voxels in the OB. Percentages of activation of all the maps, including amyl acetates, hexanal, and seven mechanical maps, were calculated. Since the breathing rate is ~1.5 Hz (see Fig. 7*B*) and tidal volume is ~1 ml in the anesthetized rat, a mechanical map of 1.5 Hz/1 ml was presented to be compared with the activation fraction of two odor maps (Fig. 2*C*).

The method for generating SCC values was referred to in previous studies (Ramsden et al., 2001; Xu et al., 2003). Briefly, SCC values are computed on a voxel-by-voxel basis by converting activation maps into

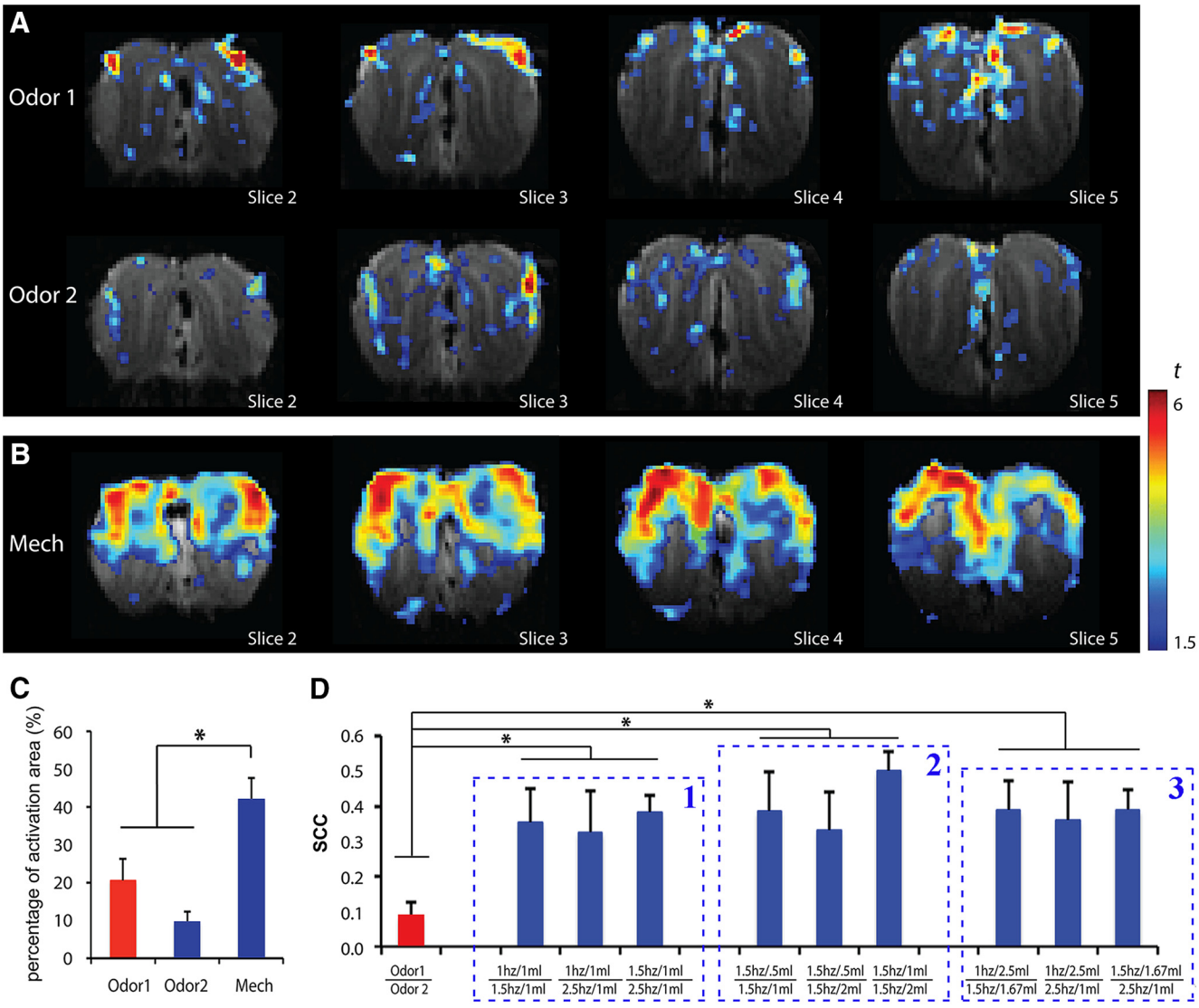

Figure 2. The activity patterns in the OB evaluated by BOLD-fMRI. ***A***, ***B***, Patterns from individual rat evoked by (***A***) different odorants (Odor 1: amyl acetate; Odor 2: hexanal) in the OB and (***B***) by airflow mechanical stimulation. Activation voxels displayed with warmer colors indicate stronger activations. ***C***, Activation rate in the OB to three different stimuli. ***D***, The SCCs between different maps, including between two odor maps (Odor 1 | Odor 2), between each of the two mechanical maps within Model I (1 Hz/1 ml | 1.5 Hz/1 ml, 1 Hz/1 ml | 2.5 Hz/1 ml, and 1.5 Hz/1 ml | 2.5 Hz/1 ml), Model II (1.5 Hz/0.5 ml | 1.5 Hz/1 ml, 1.5 Hz/0.5 ml | 1.5 Hz/2 ml, and 1.5 Hz/1 ml | 1.5 Hz/2 ml), and Model III (1 Hz/2.5 ml | 1.5 Hz/1.67 ml, 1 Hz/2.5 ml | 2.5 Hz/1 ml, and 1.5 Hz/1.67 ml | 2.5 Hz/1 ml). Unpaired *t* test, $^*p < 0.05$.

binary maps in which the value of a single voxel is either 1 (above threshold) or 0 (below threshold). When performing SCC calculations, only the voxels within the OB ROI were taken into account. For comparison between two different maps, a given voxel must belong to one of the four categories: [1, 1], [1, 0], [0, 1], or [0, 0]. $N_{[1,1]}$, $N_{[1,0]}$, $N_{[0,1]}$, and $N_{[0,0]}$ are the total number of voxels in the corresponding categories. If $N_{[1,1]} * N_{[0,0]} > N_{[1,1]} * N_{[1,0]}$, SCC is mathematically defined as follows (Cole, 1949):

$$SCC = \frac{N[1,1]N[0,0] - N[1,0]N[0,1]}{(N[1,0] + N[1,1])(N[1,0] + N[0,0])}$$

Absolute values of the SCC track with the χ^2 statistic and SCC values >0.2 are considered highly significant ($p < 0.01$) given the number of voxels ($N = 3408 \pm 67$) in the maps in this study. The SCCs between two odor maps and mechanical maps within the same model were calculated. Unpaired *t* test was performed to compare activation rates and SCC differences between different map pairs. SCC and activation rate results are presented as mean ± SE (Fig. 2*C*,*D*). A *p* value of <0.05 was considered statistically significant.

Due to the unfeasibility of performing all experimental paradigms on the same animal, voxel-by-voxel quantitative comparisons (e.g., SCC analysis) could not be performed. Instead, we separated the OB slice into 8, 16, and 32 parts slice by slice to perform correlations among these maps. For each OB slice, central line (Fig. 3*A*, green lines), dorsal site, and ventral site (Fig. 3*A*, red dots) were estimated according to the shape of the OB and alignment of different layers on MRI anatomical images. The intersection point between the central line and the dorsal-ventral site connection line was considered center of the OB slice (Fig. 3*A*, green dots). Then, the OB slice was divided into equal parts around the lines radiating from the center site. For example, the angle of each two adjacent radiation lines was 22.5° (360 ÷ 16), when dividing the OB slice into 16 parts. Since the odor maps are quite similar among glomerular, mitral cell, and granular cell layers (Li et al., 2014), all the layers of the OB within one part were reasonably put together for map similarity analysis. Each part was numerically labeled. The averaged response of each part was calculated, and then was aligned in numerical order (Fig. 3*B*–*D*). Considering the distortion and variation in the first and last slices, we combined unfolded activation bars from slices 2–5 as 8 × 4, 16 × 4, and 32 ×

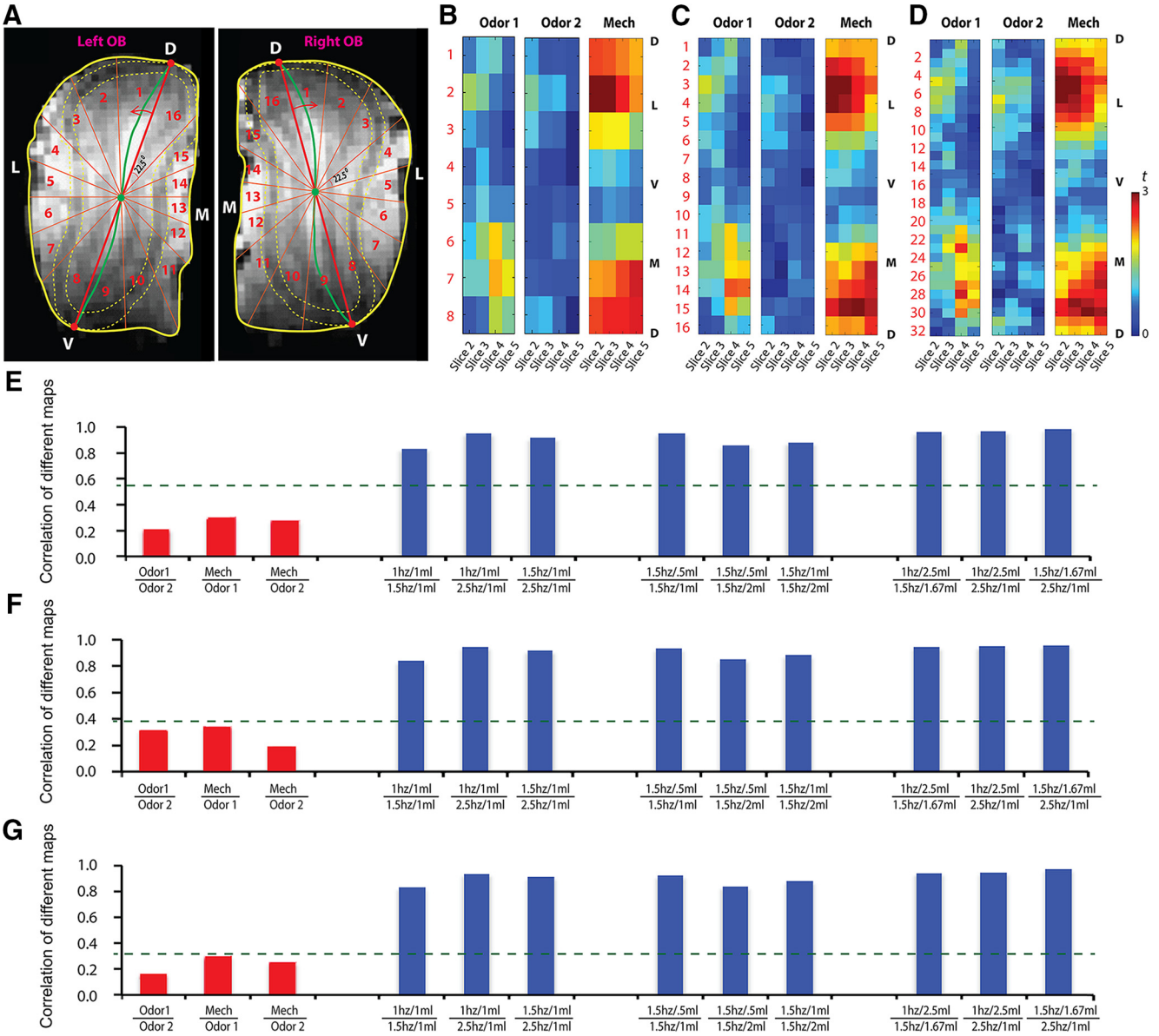

Figure 3. Similarity analysis among odor maps and mechanical maps in the OB. ***A***, One example of how the OB slice was divided into 16 parts. ***B–D***, Averaged recombined pattern of two odor maps and mechanical map, created by dividing each OB slice into 8 parts (***B***), 16 parts (***C***), and 32 parts (***D***). Warm colors indicated high activation. D, Dorsal; L, lateral; V, ventral; M, medial. ***E–G***, Correlation coefficient between patterns reconstructed from 8 parts (***E***), 16 parts (***F***), and 32 parts (***G***). The green lines indicated statistical cutoffs at $p = 0.001$.

4 matrices. All of the combined 2-D patterns to the same stimulation from different animals were averaged. Two-dimensional correlation coefficients between each two different averaged combined matrixes were calculated, including between two odor maps, between odor maps and mechanical maps, and between different mechanical maps.

LFP data analysis. LFP signals (1–100 Hz) were filtered from raw data by Spike2 (Cambridge Electronic Design), binned with a width of 1 s (2000 sample points), and the power spectral density with a resolution of 0.25 Hz (same resolution as fMRI data) was calculated with the Fourier transform. Three frequency bands of LFP (1–12 Hz, θ band; 13–34 Hz, β band; and 35–100 Hz, γ band) were selected as in previous studies (Kay and Freeman, 1998; Gelperin, 2006; Li et al., 2014), and then collapsed to one dimension to generate time courses. Specifically, frequency spectral of the θ band was calculated with Fourier transform. To calculate the signal change, temporal resolution of LFP signals was downsampled to 4 s (i.e., points within every 4 s were binned and averaged as one data point), generating a temporal resolution the same as BOLD signals. Therefore, the downsampled LFP time course contained eight data points during the rest period (32 s before stimulation), four during the activation period (16 s during stimulation), and 20 during the recovery period (80 s after stimulation). The baseline (S_{baseline}) was generated by averaging the downsampled LFP signal during the rest period (binned data points 1–8), and was subtracted from every binned data point in the stimulation stage to generate signal differences [$\Delta S(n) = S(n) - S_{\text{baseline}}$, where $S(n)$ represents signal of the n-th point in the binned data series]. Then, signal differences were divided by the baseline to generate relative signal changes [$\Delta S(n)/S_{\text{baseline}}$]. The LFP signal changes during the stimulation stage (16 s during stimulation, binned data points 9–12) were averaged as response intensities, which were subsequently averaged across trials. The response intensity was analyzed similarly to the fMRI data described above.

Physiological data analysis. EEG data were filtered at δ (1–3 Hz), θ (4–7 Hz), α (8–13 Hz), β (14–25 Hz), and γ (25–100 Hz) bands for power analysis by using previous studies as references (Hughes, 2008; Buechel et al., 2011). Averaged respiratory rates and heart rates of each animal at both baseline and stimulation were calculated for presentation (see Fig. 7*B*,*D*). For each animal, respiratory rates, heart rates and EEG signals of all trials were normalized: signals were subtracted by the baseline before

being divided by the difference between stimulation state and baseline. Normalized signals from all trials in all animals were averaged, and then analyzed with unpaired *t* test to evaluate differences between stimulating state (30 s during stimulation) and resting state (baseline, 60 s before stimulation).

Results

General features of the activity patterns elicited by odorant and airflow in the OB

Recent reports have revealed that airflow and odor sensing share a molecular signal transduction pathway in the OSNs (Grosmaitre et al., 2007; Connelly et al., 2015). Therefore, the OB should be activated by airflow. In this report, we aimed to reveal the airflow map and compare it with the odor map. The two odorant-elicited patterns are specific in the OB, with strongest signals in the glomerular layer (Fig. 2*A*; Odor 1: amyl acetate; Odor 2: hexanal), which is consistent with previous MRI studies, including ours, in rodents (Xu et al., 2003; Li et al., 2014; Poplawsky et al., 2015; Murphy et al., 2016; Sanganahalli et al., 2016). The airflow map showed that responses of the OB to mechanical stimulation were nearly uniform (Fig. 2*B*; with same threshold of odor maps). The signals induced by mechanical stimulation were robust and generally located in the olfactory nerve and glomerular layers, consistent with the neuroanatomical connections from the OE to the OB.

Statistical analyses showed that activation rates in the airflow mechanical map (42 ± 0.056%) were significantly higher than those in the odor maps (20 ± 0.057% for Odor 1 and 10 ± 0.027% for Odor 2; Fig. 2*C*; unpaired *t* test: airflow and Odor 1, $p = 0.028$; airflow and Odor 2, $p = 0.002$; Odor 1 and Odor 2, $p = 0.122$). This reveals that a more extensive activation by the airflow stimuli was elicited than those by odor stimuli in the OB. For pattern comparison, SCCs of odor maps and mechanical maps were calculated. We found that the SCC between two different odor maps (0.088 ± 0.039) was quite small, and significantly lower than those in each of the two mechanical maps (~0.4; Fig. 2*D*, red column compared with blue columns). To further examine the similarity between odor-activation and airflow-activation patterns, correlation analysis was performed on the averaged recombined 2-D maps induced by two odors and airflow stimuli. Recombined *t*-value patterns of two odor maps and one mechanical map—created by dividing each OB slice into eight parts (Fig. 3*B*), 16 parts (Fig. 3*C*), and 32 parts (Fig. 3*D*)—were presented. Interestingly, the asymmetrical lateral and medial distributed patterns were found in the reconstructed *t*-value maps (Fig. 3*B–D*). Our results showed that the patterns elicited from these three different methods were similar. The 2-D correlation coefficients for the reconstructed maps (Odor 1 vs Odor 2; mechanical vs odor) showed that their similarities were low, while the topographies of the mechanical maps under different experimental conditions were highly similar (i.e., the heights of the blue columns are much larger than the significant level, while those of red columns are not; Fig. 3*E–G*). These results demonstrated that the activity patterns elicited by chemical and mechanical stimulations in the OB are significantly different.

The representation of different stimulating conditions in the OB

Since the topographies of the mechanical maps, as revealed by 2-D correlation coefficients, are highly similar, the question of how the respiratory parameters are represented by the activity patterns in the OB was investigated. For this purpose, we investigated BOLD responses of the rat OB to three mechanical stimulation paradigms (Fig. 1).

It is well known that as an animal samples air through sniffing, the breathing rate increases. The experimental results here showed that with the stroke volume set at 1.0 ml, BOLD responses increased with sampling frequency (Fig. 4*A*, maps in different rows) while the topography of the activity patterns remained nearly the same (Fig. 2*D1*). The time courses of the BOLD signals showed that the response dynamics are similar and that higher frequencies elicited stronger responses, as shown in the airflow maps (Fig. 4*A*, *B*). Statistical results indicated that BOLD signals increased significantly with stimulation frequency (Fig. 4*C*; ANOVA, $F_{(2,12)} = 17.78$, $p = 0.00026$; paired *t* test: 1 Hz/1 ml and 1.5 Hz/1 ml, $p = 0.034$; 1.5 Hz/1 ml and 2.5 Hz/1 ml, $p = 0.026$; 1 Hz/1 ml and 2.5 Hz/1 ml, $p = 0.002$).

Stroke volume is another basic parameter for respiration. With a constant "breathing" frequency, the intensity of the activity pattern increases with stroke volume, but the topography of these patterns was maintained (Fig. 2*D2*). Similar to the case of constant "breathing" frequency, the corresponding time courses of the BOLD signals at these conditions showed that the response dynamics are equivalent and the peak intensity increases significantly with stroke volume (Fig. 4*D–F*; ANOVA, $F_{(2,12)} = 14.15$, $p = 0.0007$; paired *t* test: 1.5 Hz/0.5 ml and 1.5 Hz/1 ml, $p = 0.017$; 1.5 Hz/1 ml and 1.5 Hz/2 ml, $p = 0.04$; 1.5 Hz/0.5 ml and 1.5 Hz/2 ml, $p = 0.0003$).

In the third paradigm, the stimulation frequency and stroke volume were varied simultaneously with the total stimulating strength fixed (volume × frequency = constant). The results showed that both the mechanical patterns and the response intensities were similar to each other (Figs. 2*D3*, 4*G*). The time courses of the BOLD responses at these stimulus conditions highly overlapped with each other (Fig. 4*H*). Statistical analysis results showed that BOLD signals had no significant changes when the mechanical stimulation strength was fixed (Fig. 4*I*; ANOVA, $F_{(2,15)} = 0.042$, $p = 0.959$; paired *t* test: 1 Hz/2.5 ml and 1.5 Hz/1.67 ml, $p = 0.33$; 1.5 Hz/1.67 ml and 2.5 Hz/1 ml, $p = 0.43$; 1 Hz/2.5 ml and 2.5 Hz/1 ml, $p = 0.47$).

Furthermore, the relationships between different mechanical maps were analyzed. The SCCs between two mechanical maps within the same model were calculated and compared. The group results showed that the SCCs (>0.3) of all mechanical map comparisons were high and highly significant, implying high similarity among all airflow-induced OB response maps (Fig. 2*D*, all blue columns). Additionally, we found that the 2-D correlation coefficients (>0.8) between each two recombined mechanical maps by all three separating methods (dividing each OB slice into 8, 16, and 32 parts) were highly significant (Fig. 3*E*, *F*, blue columns). Also, group data show no significant differences in these 2-D correlation coefficients (Fig. 3*E*, *F*, blue columns). Similar to the SCC, the high correlations of all mechanical map comparisons imply high similarity among all airflow maps in the OB. In summary, statistical analysis showed that the topographies of activity patterns elicited under these three paradigms are highly similar.

The LFP signals in different stimulating paradigms

We have shown that the BOLD patterns in the OB can partially encode respiratory information. However, there are two remaining concerns: (1) it is unclear how BOLD signal correlated with the signal from a gold-standard measurement for activity, since BOLD signal is not a direct measurement of neural activity; and (2) it is unclear how the elicited pattern can discriminate between different total airflows, but, unexpectedly, not between different subparameters (breathing frequency and stroke volume). To clarify these concerns, LFP, which has a much higher temporal

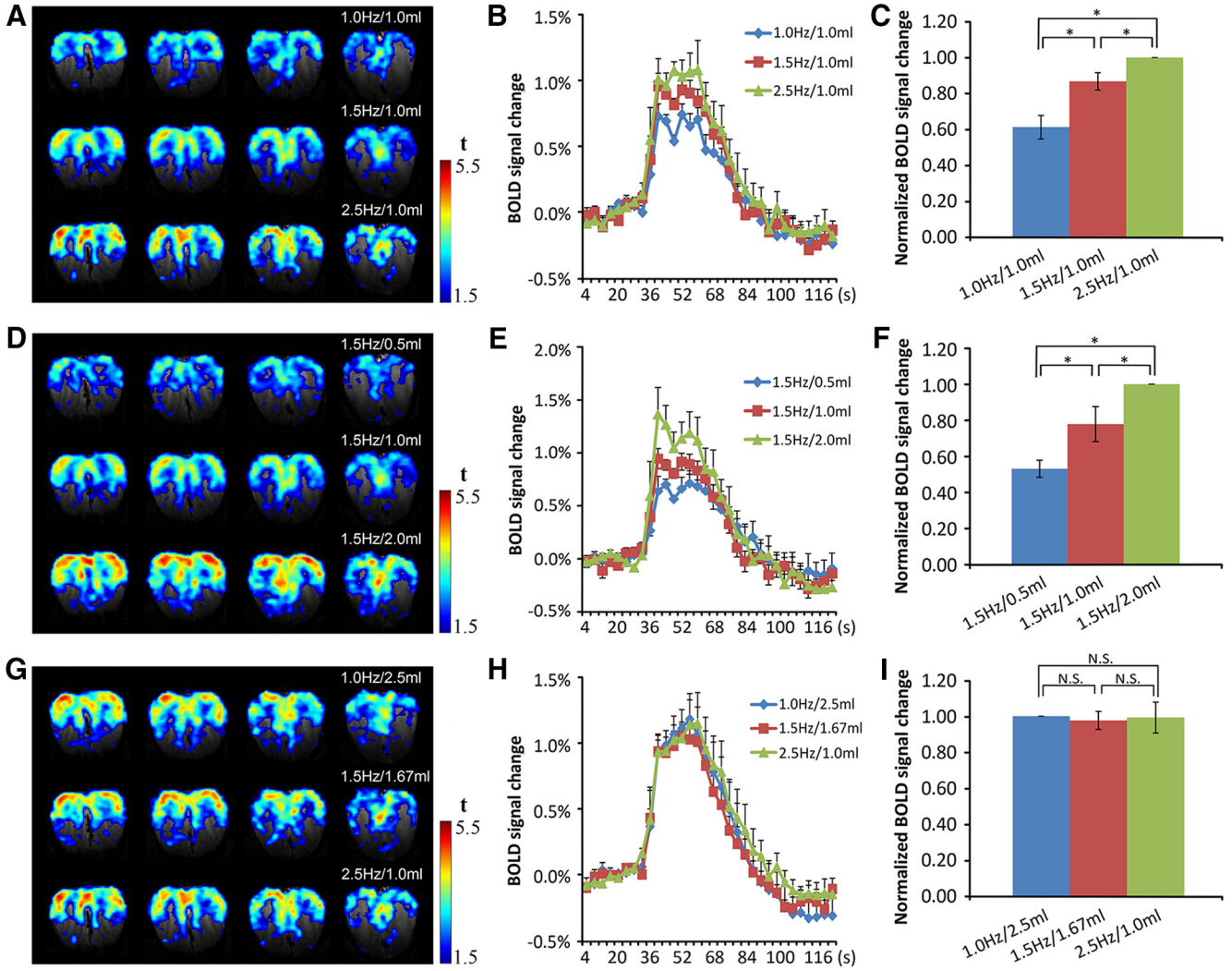

Figure 4. BOLD responses to different mechanical stimuli in the OB. ***A–C***, Model I: The elicited BOLD patterns (***A***), corresponding time courses of BOLD signals (***B***), and statistical analysis (***C***). Data were normalized to the response of the 2.5 Hz/1.0 ml stimulation. Paired *t* test, $*p < 0.05$; $n = 5$/one-way ANOVA, $F_{(2,12)} = 17.78$, $*p < 0.05$. ***D–F***, Model II: the elicited BOLD patterns (***D***), corresponding time courses of BOLD signals (***E***), and statistical analysis (***F***). Data were normalized to the response of 1.5 Hz/2.0 ml stimulation. Paired *t* test, $*p < 0.05$; $n = 5$/one-way ANOVA, $F_{(2,12)} = 14.15$, $*p < 0.05$. ***G–I***, Model III: the elicited BOLD patterns (***G***), corresponding time courses of BOLD signals (***H***), and statistical analysis (***I***). Data were normalized to the response of 2.5 Hz/1.0 ml stimulation. Paired *t* test, N.S, $p > 0.5$; $n = 6$/one-way ANOVA, $F_{(2,15)} = 0.042$, N.S, $p > 0.5$. Error bar, SE.

resolution, was recorded in the glomerular layer under identical experimental conditions to verify the BOLD-fMRI findings (Fig. 5*A*, top row). The raw LFP data were filtered and the signal in θ, β, and γ bands were extracted and analyzed (Fig. 5*A*, lower rows). The time courses showed that the power for the three LFP bands increased at the onset of the mechanical stimulation (Fig. 5*B*). The powers of the different bands increased differently (peak amplitude $\beta > \gamma > \theta$), and with different dynamics: β-band signal increased rapidly at the stimulation onset but dropped rapidly before the stimulation ends; γ-band signal was maintained during the entire period of stimulation and needed a few minutes to recover to baseline; θ-band signal first increased and then, with the stimulation time course, decreased.

Considering the response stability and amplitude, the γ-band signals were used to compare responses in the three different stimulation paradigms. The results showed that the signal increased significantly with breathing frequency when the stroke volume was fixed (Fig. 5*C*; paradigm I, ANOVA, $F_{(2,27)} = 7.26$, $p = 0.003$; paired *t* test: 1 Hz/1 ml and 1.5 Hz/1 ml, $p = 0.038$; 1.5 Hz/1 ml and 2.5 Hz/1 ml, $p = 0.028$; 1 Hz/1 ml and 2.5 Hz/1 ml, $p = 0.0006$), and similarly with stroke volume when the frequency was fixed (Fig. 5*D*; paradigm II, ANOVA, $F_{(2,27)} = 50.5$, $p = 7.5 \times 10^{-10}$; paired *t* test: 1.5 Hz/0.5 ml and 1.5 Hz/1 ml, $p = 0.003$; 1.5 Hz/1 ml and 1.5 Hz/2 ml, $p = 7.3 \times 10^{-5}$; 1.5 Hz/0.5 ml and 1.5 Hz/2 ml, $p = 3.0 \times 10^{-7}$). However, γ-band signals did not change with equal airflow (Fig. 5*E*; paradigm III, ANOVA, $F_{(2,27)} = 0.52$, $p = 0.60$; paired *t* test: 1 Hz/2.5 ml and 1.5 Hz/1.67 ml, $p = 0.21$; 1.5 Hz/1.67 ml and 2.5 Hz/1 ml, $p = 0.25$; 1 Hz/2.5 ml and 2.5 Hz/1 ml, $p = 0.48$). Overall, these LFP findings of mechanical response characteristics in the OB are consistent with those evaluated by fMRI.

The phenomenon that the BOLD signal only reflects total airflow volume, as we have observed, could be due to the temporal resolution of BOLD signal that is too low to distinguish the changing variables. Since the θ band covers the tested range of breathing frequencies and is strongly related to sniffing (Macrides and Chorover, 1972; Onoda and Mori, 1980; Ravel and Pager, 1990), the power spectra of the band at different stimulation conditions were analyzed to verify our presumption. The results clearly demonstrated that the main frequency of the LFP

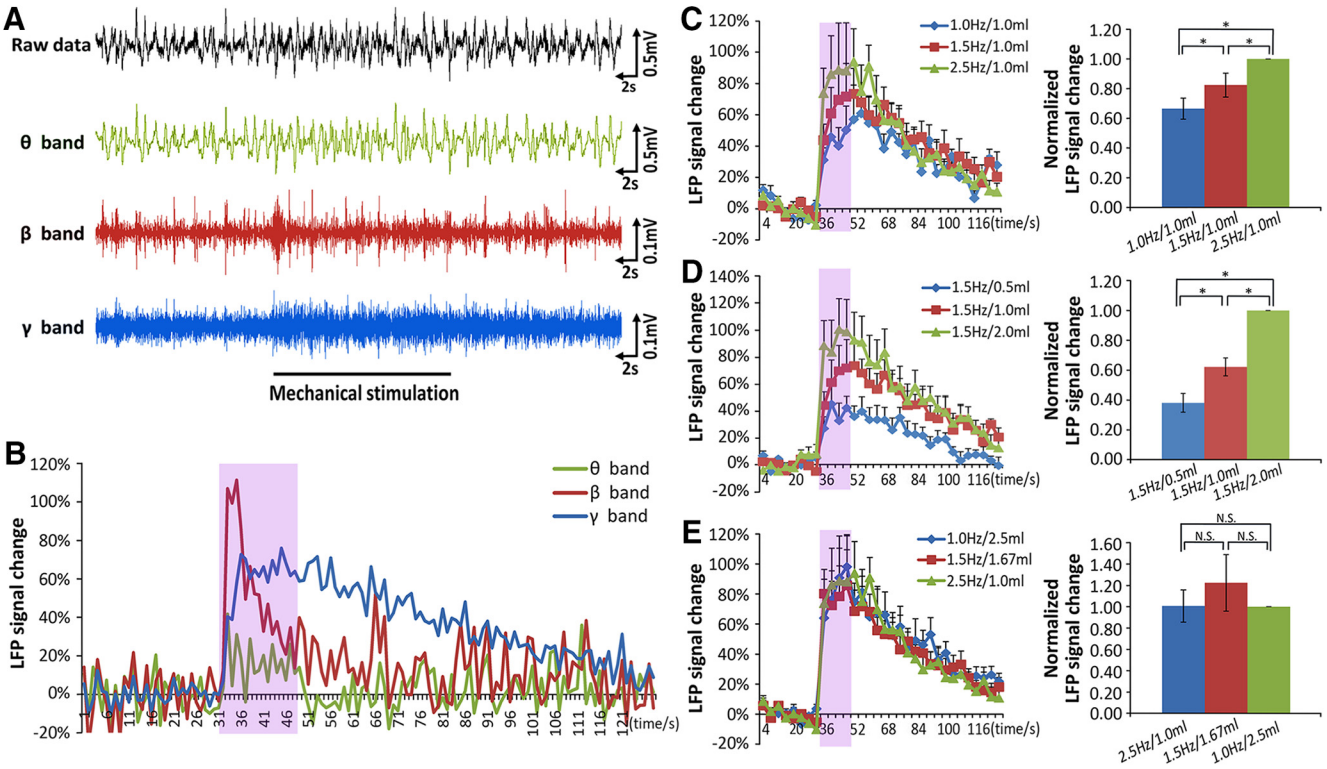

Figure 5. LFP in the OB under different mechanical stimulation conditions. ***A***, An example of raw LFP signals and filtered signals for three different frequency bands (θ band: 1–12 Hz; β band: 12–35 Hz; γ band: 35–100 Hz) elicited by mechanical stimulus. ***B***, The time courses of the LFP signals induced by mechanical stimulation in ***A***. ***C***, The γ-band signal change in the OB to Model I conditions. Data were normalized to the response of 2.5 Hz/1.0 ml. Paired *t* test, $^*p < 0.05$, $n = 10$/one-way ANOVA, $F_{(2,27)} = 7.26$, $^*p < 0.05$. ***D***, The γ-band response to the Model II conditions. Data were normalized to the response of 1.5 Hz/2.0 ml. Paired *t* test, $^*p < 0.05$, $n = 10$/one-way ANOVA, $F_{(2,27)} = 50.5$, $^*p < 0.05$. ***E***, The γ-band signal to the Model III conditions. Data were normalized to the response of 2.5 Hz/1.0 ml. Paired *t* test, N.S, $p > 0.5$, $n = 10$/one-way ANOVA, $F_{(2,27)} = 0.52$, N.S, $p > 0.1$. Error bar, SE.

followed the breathing frequency closely in paradigm I (Fig. 6*A*), during which the frequency was changed, but remained the same in paradigm II (Fig. 6*B*), when the frequency was fixed. Therefore, the main frequency of the LFP θ band in the OB was coupled with the breathing frequency, suggesting that the OB is able to encode airflow-frequency information. This is consistent with a previous study that nasal airflow drives respiration-coupled spiking on both mitral and tufted cells (Phillips et al., 2012).

Physiological conditions affected by breathing parameters

Physiological conditions can change breathing patterns (Dejours et al., 1970; Philippot et al., 2002). Here we examined the effects of breathing on physiological conditions by monitoring the respiratory rate, heart rate, and EEG signals during resting and stimulating states. Our results revealed that the respiratory rate for a group of eight animals decreased significantly during the 1.0 Hz/2.5 ml mechanical stimulating state (Fig. 7*A*; unpaired *t* test, $p = 0.011$). Also, the respiratory rates of each rat at resting state were faster than those at stimulating state (Fig. 7*B*), although the differences were animal-dependent. The averaged normalized heart rates of eight rats were also compared between resting and stimulating states, and we found a statistically significant decrease during stimulating state (Fig. 7*C*; unpaired *t* test, $p = 0.023$). Individually, of the eight animals, the heart rates of seven decreased while only one remained constant during stimulation (Fig. 7*D*). EEG data were filtered at δ, θ, α, β, and γ bands before comparing their powers between resting and stimulating states. It was found that the normalized power of β waves was significantly weaker during stimulation (Fig. 7*E*; unpaired *t* test, $p = 0.01$), while the other bands showed no significant differences between "active" and "rest" states (Fig. 7*F*; unpaired *t* test: δ, $p = 0.072$; θ, $p = 0.061$; α, $p = 0.341$; γ, $p = 0.30$).

Discussion

Topographies of odor and airflow maps

Activity patterns in the OB evoked by nasal airflow were more broadly distributed, while those elicited by odorants were odor-specific and more sparsely distributed (Fig. 2). The patterns of odor maps were consistent with those of our previous studies and those of other groups (Xu et al., 2000b; Kida et al., 2002; Wachowiak and Shipley, 2006; Martin et al., 2007; Murphy et al., 2016). Odor detection depends on a large family of ORs expressed in the OSNs. Each OSN expresses a single OR type, which determines its response profile and central targets in the OB (Buck and Axel, 1991; Zhang et al., 2007). A given type of OSN converges onto a pair of glomeruli in the lateral and medial sides of the OB. A given odor activates a specific subset of OSN types and thus a specific subset of glomeruli (Zhao et al., 1998; Malnic et al., 1999; Mori et al., 2006). Indeed, different odors evoke globally specific and locally overlapping activity patterns across the OB, as revealed by different techniques (Uchida et al., 2000; Xu, 2001; Soucy et al., 2009).

Unlike chemical patterns in the OB, mechanical patterns have never been reported previously. Strikingly different from the odor maps, the mechanical maps under different airflow conditions are much more uniformly distributed across the OB with highly similar topographies, making the feature of the airflow maps monotonous or stereotyped. *In vitro* data have revealed that ~70% of OSNs in the septal organ and ~50% of OSNs in the main OE are capable of sensing mechanical stimulation (Gros-

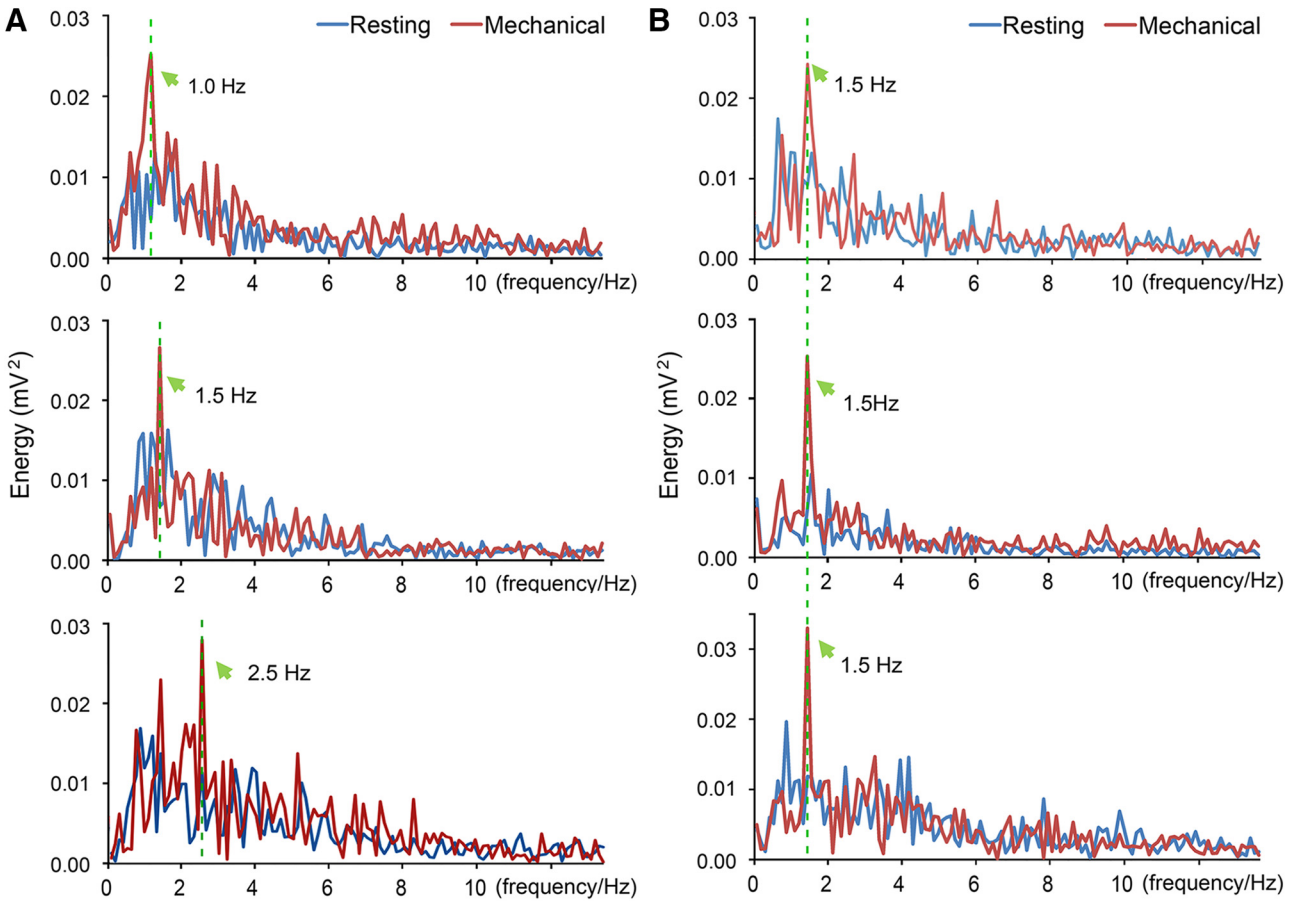

Figure 6. The main frequency of the LFP θ band was coupled with the mechanical airflow frequency in the endotracheal intubation animal. ***A***, Frequency spectra of the θ band at different stimulus frequencies (top, 1.0 Hz/1.0 ml; middle, 1.5 Hz/1.0 ml; bottom, 2.5 Hz/1.0 ml). ***B***, Frequency spectra of the θ-band signal at different stimulus strengths with the same frequency (top, 1.5 Hz/0.5 ml; middle, 1.5 Hz/1.0 ml; bottom, 1.5 Hz/2.0 ml). The frequency spectra during and before stimulation (resting) were presented with red and blue lines respectively. The main frequencies were indicated by green arrows.

maitre et al., 2007), and thus potentially serve as mechanosensors. Responses from OSNs expressing normal and genetically altered ORs have revealed that ORs are necessary and sufficient for mechanical response of the host cells, and that the downstream signal transduction cascade is the basis for this response (Connelly et al., 2015). Further, OSNs expressing an inactivated OR (OR-I7) do not have any spontaneous activity and OSNs expressing different ORs have significantly different basal activity (Connelly et al., 2013). Therefore, when there is airflow, the mechanical responses of a given type of OSN could be coordinated to alter the activity in the corresponding glomeruli. With the spatial resolution of our BOLD-fMRI, the observed signal is the summed activity from different types of OSNs. Additionally, the asymmetrical medial and lateral activity patterns could be due to the localization of the paired glomeruli in the same OB for a given type of OSN, with the lateral one located more dorsally and anteriorly, and the medial one located more ventrally and posteriorly (Vassar et al., 1994; Mombaerts et al., 1996).

Intensities of odor and airflow maps

It is rather intuitive and evident that the intensity of the odor maps increases with odor concentration, as observed previously (Rubin and Katz, 1999; Schafer et al., 2005; Li et al., 2014). Activated voxels in airflow maps also increase with airflow, either through increases in tidal volume or breathing frequency as revealed by BOLD-fMRI (Fig. 4) and the LFP γ band (Fig. 5). These data demonstrated that the OB is able to encode information of airflow intensity. Similar to odor maps, the strongest signals of the airflow map are also localized in the glomerular layer of the OB. This is because the airflow sensing and odor sensing by OSNs share the molecular signal transduction pathway and the downstream neurocircuits from the OE to the OB.

Nasal airflow information is reflected by BOLD and LFP signals

Our BOLD-fMRI data demonstrated that neural activity in the OB only reflects the total volume of airflow (Fig. 4). However, the main frequency of the LFP θ band follows the breathing frequency precisely (Fig. 6). The LFP γ band changed with total volume (Fig. 5). The BOLD signal is an indirect measurement of neural activity in large volumes of tissue, with second temporal resolution and submillimeter spatial resolution (Heeger and Ress, 2002; Logothetis, 2008), while the LFP from microelectrode monitors directs neural activity in much smaller volumes of tissue, with millisecond temporal resolution at single-cell resolution (Buzsáki et al., 2012). The LFP, but not the slow hemodynamic-dependent BOLD signal, can capture the fast temporal information of airflow under our experimental conditions. In summary, the broadly distributed mechanical pattern is robust, topographically simple, and dependent on the stimulation paradigm.

A number of studies have shown that the electrical activities in the OB are synchronized with breathing rhythm (Macrides and Chorover, 1972; Onoda and Mori, 1980; Ravel and Pager, 1990;

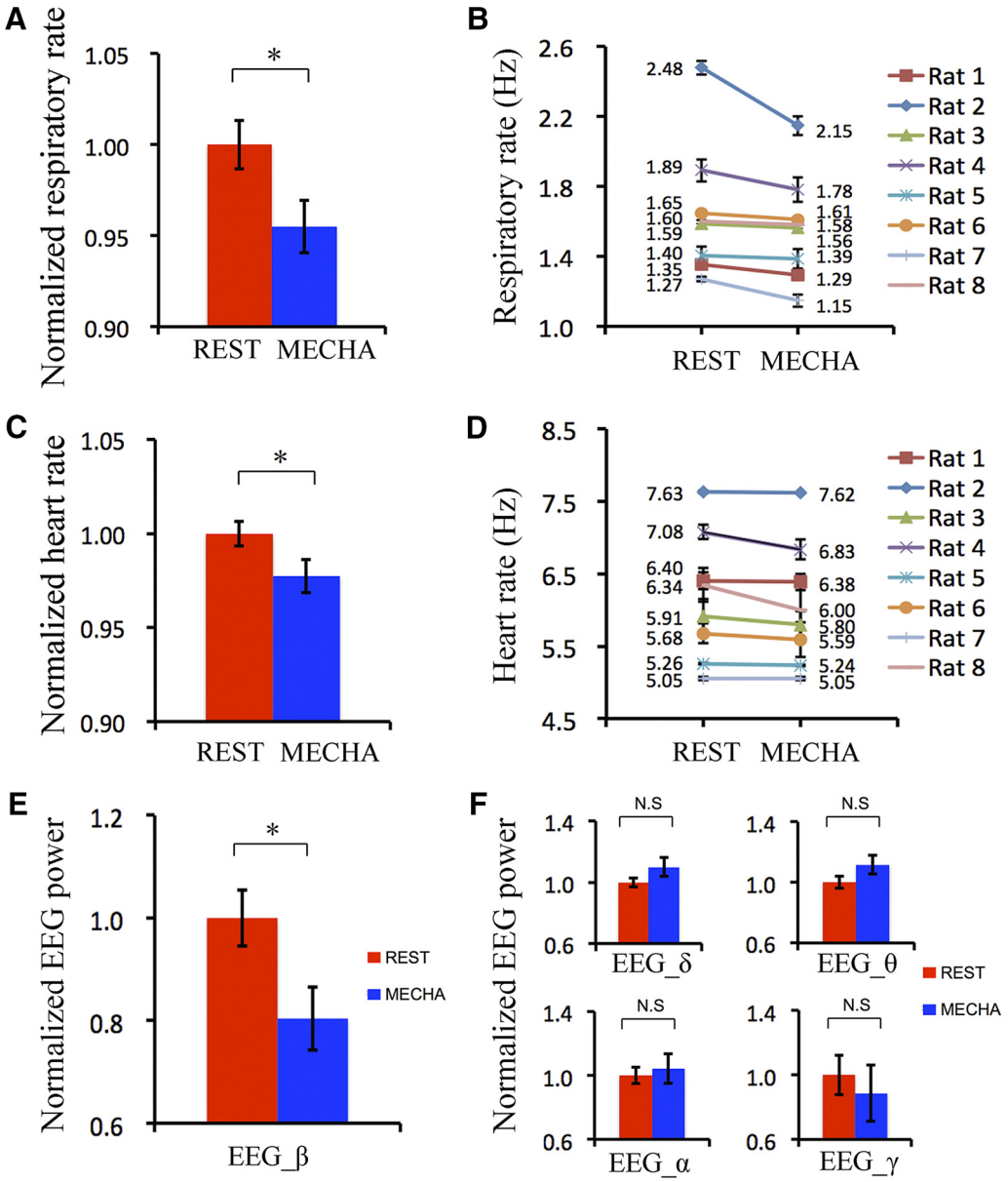

Figure 7. Respiratory rate, heart rate, and EEG were influenced by mechanical rhythm. ***A***, ***B***, Respiratory rates at resting state and mechanical state as a group (***A***) and as individuals (***B***). ***C***, ***D***, Heart rates at resting state and mechanical state as a group (***C***) and as individuals (***D***). ***E***, β Band of EEG powers at resting state and mechanical state as a group. ***F***, Powers of δ band, θ band, α band, and γ band of EEG at resting state and mechanical state. Unpaired *t* test, $*p < 0.05$; N.S, $p > 0.05$. Error bar: SE. The mechanical stimulation was 1.0 Hz/2.5 ml.

Carey et al., 2009; Phillips et al., 2012). Otherwise, the OSNs do not respond to airflow, and the rhythmic activity in the OB uncouples from respiration in cnga2 knock-out mice (Grosmaitre et al., 2007). The main frequency of the LFP θ band in the OB was coupled with airflow frequency in the nasal cavity of endotracheal-cannulated animals (Fig. 6), which agrees with previous studies and supports the hypothesis that the OSN mechanosensitivity drives the rhythmicity of the OB (Grosmaitre et al., 2007; Connelly et al., 2015).

Due to animal ethics and technical limitations, several issues remain to be addressed. First, the small 10-mm-diameter circular surface coil centered closely on the skull above the OB yielded high but distance-dependent SNR MRI images, resulting in dorsal-dominating activity patterns. Second, the airflow to the nasal cavity, controlled by a ventilator connected to the opened trachea, is artificial. The observed response occurred at the condition from no airflow to regular airflow. Therefore, the results would be overestimated, due to the lack of adaptation. Third, the investigated airflow frequency was for regular breathing, between 1 and 2.5 Hz, limiting its evaluation in sniffing behavior. Last, with the opened trachea surgery, we could not investigate the effects of regular breathing on the brain and physiological states of awake animals by controlling respiratory parameters. The effects observed under 1.5 g/kg urethane should be considerably smaller than that in awake animals.

Possible functions of airflow-induced activities in the olfactory system

Human breathing can be involuntarily changed when you enter an emotional state. It can also be consciously controlled when you intentionally attempt to calm down from a disturbed condition. In practicing meditation, yoga, or Taoism, subjects maintain a deepened slow and regular breath, which significantly changes brain and body states (Tang et al., 2009; Bhaduri and Ghosh, 2016). A number of recent publications have dem-

onstrated a direct correlation between respiration and brain activity in rodents and humans, including effects of nasal respiration on memory and behavior (Ito et al., 2014; Heck et al., 2016; Nguyen Chi et al., 2016; Zelano et al., 2016; Biskamp et al., 2017). These are not surprising because the OB projects heavily to the amygdala, entorhinal, and piriform cortices, all key components of the limbic system, which plays important roles in regulation of emotion, olfaction, and the autonomic nervous system. Indeed, the OSN mechanosensitivity and the incurred changes in the olfactory system can affect brain (i.e., OB) and physiological states, as our experimental data have shown (Fig. 7).

Another possible function of OSN mechanosensitivity is its role in formatting and maintaining neuroanatomical connections in the olfactory system. Olfactory deprivation has been shown to produce substantial alterations in neurophysiology of OSNs and neurochemistry of the olfactory system in both newborn and adult animals (Guthrie et al., 1990; Wilson and Sullivan, 1995; Shipley and Ennis, 1996; Zou et al., 2004; Kass et al., 2013). A previous study reported that olfactory deprivation reduces the number, dendritic length, and spine density of newborn granule cells (Saghatelyan et al., 2005). Studies also indicate that experience of simple odorant exposures can influence the subsequent odor activity patterns in the OB (Buonviso and Chaput, 2000; Spors and Grinvald, 2002), and enhance the selectivity of mitral/tufted cells (Fletcher and Wilson, 2003). Therefore, a basal odor-independent activity in OSNs evoked by airflow might contribute to the establishment and maintenance of proper neural connections in the olfactory system, though none of these studies addressed this specifically.

Last, the possible function of OSN mechanosensitivity is for more accurate coding of odor information (Grosmaitre et al., 2007). The total amount of odorants entering the nasal cavity and the components of an odor mixture absorbed by the respiratory and the olfactory epithelia are strongly dependent on breathing patterns (Sobel et al., 1998a). Therefore, the same odor sample may activate the olfactory system at different levels, depending on the breathing parameters. Since the olfactory system responds to both odorant and mechanical stimuli, the interaction of these two information sources in the brain always occurs when an animal breathes or sniffs to sense odor. Studies on humans have revealed that sniffing, with or without odorant, activates primarily the anterior central regions of cerebellum, the piriform cortex of the temporal lobe, and the medial posterior orbitofrontal gyri of the frontal lobe, while smelling activates the anterior-lateral orbitofrontal gyri of the frontal lobe, and the posterior lateral cerebellum (Sobel et al., 1998a,b). These two types of information might be dissociated from each other.

Conclusions

In this report, the effects of different airflow paradigms on the OB and physiological states were studied in rats. We found that airflow-evoked patterns in the OB were global and stable. The pattern intensity, not the topography, was dependent on the stimulation paradigms. Also, a regular airflow in the nasal cavity significantly decreased EEG power in the β band, and mildly decreased physiological signals of the heart rate and the spontaneous respiratory rate. These results suggest several possible fundamental functions of mechanical perception in the olfactory system and the brain.

References

Bandettini PA (2012) Twenty years of functional MRI: The science and the stories. Neuroimage 62:575–588. CrossRef Medline

Bhaduri A, Ghosh D (2016) Quantitative assessment of heart rate dynamics during meditation: An ECG based study with multi-fractality and visibility graph. Front Physiol 7:44. CrossRef Medline

Biskamp J, Bartos M, Sauer JF (2017) Organization of prefrontal network activity by respiration-related oscillations. Sci Rep 7:45508. CrossRef Medline

Buck L, Axel R (1991) A novel multigene family may encode odorant receptors—a molecular-basis for odor recognition. Cell 65:175–187. CrossRef Medline

Buechel HM, Popovic J, Searcy JL, Porter NM, Thibault O, Blalock EM (2011) Deep sleep and parietal cortex gene expression changes are related to cognitive deficits with age. PLoS One 6:e18387. CrossRef Medline

Buonviso N, Chaput M (2000) Olfactory experience decreases responsiveness of the olfactory bulb in the adult rat. Neuroscience 95:325–332. Medline

Buzsáki G, Anastassiou CA, Koch C (2012) The origin of extracellular fields and currents—EEG, ECoG, LFP and spikes. Nat Rev Neurosci 13:407–420. CrossRef Medline

Carey RM, Verhagen JV, Wesson DW, Pírez N, Wachowiak M (2009) Temporal structure of receptor neuron input to the olfactory bulb imaged in behaving rats. J Neurophysiol 101:1073–1088. CrossRef Medline

Cole LC (1949) The measurement of interspecific association. Ecology 30:411–424. CrossRef

Connelly T, Savigner A, Ma M (2013) Spontaneous and sensory-evoked activity in mouse olfactory sensory neurons with defined odorant receptors. J Neurophysiol 110:55–62. CrossRef Medline

Connelly T, Yu Y, Grosmaitre X, Wang J, Santarelli LC, Savigner A, Qiao X, Wang Z, Storm DR, Ma M (2015) G protein-coupled odorant receptors underlie mechanosensitivity in mammalian olfactory sensory neurons. Proc Natl Acad Sci U S A 112:590–595. CrossRef Medline

Dejours P, Garey WF, Rahn H (1970) Comparison of ventilatory and circulatory flow rates between animals in various physiological conditions. Respir Physiol 9:108–117. CrossRef Medline

Firestein S (2001) How the olfactory system makes sense of scents. Nature 413:211–218. CrossRef Medline

Fletcher ML, Wilson DA (2003) Olfactory bulb mitral-tufted cell plasticity: odorant-specific tuning reflects previous odorant exposure. J Neurosci 23:6946–6955. Medline

Fontanini A, Spano P, Bower JM (2003) Ketamine-xylazine-induced slow (<1.5 Hz) oscillations in the rat piriform (olfactory) cortex are functionally correlated with respiration. J Neurosci 23:7993–8001. Medline

Gelperin A (2006) Olfactory computations and network oscillation. J Neurosci 26:1663–1668. CrossRef Medline

Grosmaitre X, Santarelli LC, Tan J, Luo M, Ma M (2007) Dual functions of mammalian olfactory sensory neurons as odor detectors and mechanical sensors. Nat Neurosci 10:348–354. CrossRef Medline

Guthrie KM, Wilson DA, Leon M (1990) Early unilateral deprivation modifies olfactory bulb function. J Neurosci 10:3402–3412. Medline

Heck DH, McAfee SS, Liu Y, Babajani-Feremi A, Rezaie R, Freeman WJ, Wheless JW, Papanicolaou AC, Ruszinkó M, Sokolov Y, Kozma R (2016) Breathing as a fundamental rhythm of brain function. Front Neural Circuits 10:115. CrossRef Medline

Heeger DJ, Ress D (2002) What does fMRI tell us about neuronal activity? Nat Rev Neurosci 3:142–151. CrossRef Medline

Hughes JR (2008) Gamma, fast, and ultrafast waves of the brain: their relationships with epilepsy and behavior. Epilepsy Behav 13:25–31. CrossRef Medline

Ito J, Roy S, Liu Y, Cao Y, Fletcher M, Lu L, Boughter JD, Grün S, Heck DH (2014) Whisker barrel cortex delta oscillations and gamma power in the awake mouse are linked to respiration. Nat Commun 5:3572. CrossRef Medline

Kass MD, Moberly AH, Rosenthal MC, Guang SA, McGann JP (2013) Odor-specific, olfactory marker protein-mediated sparsening of primary olfactory input to the brain after odor exposure. J Neurosci 33:6594–6602. CrossRef Medline

Kay LM, Freeman WJ (1998) Bidirectional processing in the olfactory-limbic axis during olfactory behavior. Behav Neurosci 112:541–553. CrossRef Medline

Kida I, Xu F, Shulman RG, Hyder F (2002) Mapping at glomerular resolution: fMRI of rat olfactory bulb. Magn Reson Med 48:570–576. CrossRef Medline

Legaspi M, Authier S, Gauvin D, Moreau M, Beauchamp G, Chaurand F,

Troncy E (2010) Respiratory safety pharmacology: concurrent validation of volume, rate, time, flow and ratio variables in conscious male Sprague-Dawley rats. Regul Toxicol Pharmacol 58:444–450. CrossRef Medline

Li B, Gong L, Wu R, Li A, Xu F (2014) Complex relationship between BOLD-fMRI and electrophysiological signals in different olfactory bulb layers. Neuroimage 95:29–38. CrossRef Medline

Lledo PM, Gheusi G, Vincent JD (2005) Information processing in the mammalian olfactory system. Physiol Rev 85:281–317. CrossRef Medline

Logothetis NK (2008) What we can do and what we cannot do with fMRI. Nature 453:869–878. CrossRef Medline

Macrides F, Chorover SL (1972) Olfactory bulb units—activity correlated with inhalation cycles and odor quality. Science 175:84–87. CrossRef Medline

Malnic B, Hirono J, Sato T, Buck LB (1999) Combinatorial receptor codes for odors. Cell 96:713–723. CrossRef Medline

Martin C, Grenier D, Thévenet M, Vigouroux M, Bertrand B, Janier M, Ravel N, Litaudon P (2007) fMRI visualization of transient activations in the rat olfactory bulb using short odor stimulations. Neuroimage 36:1288–1293. CrossRef Medline

Mombaerts P, Wang F, Dulac C, Chao SK, Nemes A, Mendelsohn M, Edmondson J, Axel R (1996) Visualizing an olfactory sensory map. Cell 87:675–686. CrossRef Medline

Mori K, Takahashi YK, Igarashi KM, Yamaguchi M (2006) Maps of odorant molecular features in the mammalian olfactory bulb. Physiol Rev 86:409–433. CrossRef Medline

Murphy MC, Poplawsky AJ, Vazquez AL, Chan KC, Kim SG, Fukuda M (2016) Improved spatial accuracy of functional maps in the rat olfactory bulb using supervised machine learning approach. Neuroimage 137:1–8. CrossRef Medline

Nguyen Chi V, Müller C, Wolfenstetter T, Yanovsky Y, Draguhn A, Tort AB, Brankačk J (2016) Hippocampal respiration-driven rhythm distinct from theta oscillations in awake mice. J Neurosci 36:162–177. CrossRef Medline

Onoda N, Mori K (1980) Depth distribution of temporal firing patterns in olfactory-bulb related to air-intake cycles. J Neurophysiol 44:29–39. Medline

Pass D, Freeth G (1993) The Rat. ANZCCART News 6:1–4.

Philippot P, Chapelle G, Blairy S (2002) Respiratory feedback in the generation of emotion. Cogn Emot 16:605–627. CrossRef

Phillips ME, Sachdev RN, Willhite DC, Shepherd GM (2012) Respiration drives network activity and modulates synaptic and circuit processing of lateral inhibition in the olfactory bulb. J Neurosci 32:85–98. CrossRef Medline

Poplawsky AJ, Kim SG (2014) Layer-dependent BOLD and CBV-weighted fMRI responses in the rat olfactory bulb. Neuroimage 91:237–251. CrossRef Medline

Poplawsky AJ, Fukuda M, Murphy M, Kim SG (2015) Layer-specific fMRI responses to excitatory and inhibitory neuronal activities in the olfactory bulb. J Neurosci 35:15263–15275. CrossRef Medline

Ramsden BM, Hung CP, Roe AW (2001) Real and illusory contour processing in area VI of the primate: a cortical balancing act. Cereb Cortex 11:648–665. CrossRef Medline

Ravel N, Pager J (1990) Respiratory patterning of the rat olfactory bulb unit activity nasal versus tracheal breathing. Neurosci Lett 115:213–218. CrossRef Medline

Rubin BD, Katz LC (1999) Optical imaging of odorant representations in the mammalian olfactory bulb. Neuron 23:499–511. CrossRef Medline

Saghatelyan A, Roux P, Migliore M, Rochefort C, Desmaisons D, Charneau P, Shepherd GM, Lledo PM (2005) Activity-dependent adjustments of the inhibitory network in the olfactory bulb following early postnatal deprivation. Neuron 46:103–116. CrossRef Medline

Sanganahalli BG, Rebello MR, Herman P, Papademetris X, Shepherd GM, Verhagen JV, Hyder F (2016) Comparison of glomerular activity patterns by fMRI and wide-field calcium imaging: implications for principles underlying odor mapping. Neuroimage 126:208–218. CrossRef Medline

Schafer JR, Kida I, Rothman DL, Hyder F, Xu F (2005) Adaptation in the rodent olfactory bulb measured by fMRI. Magn Reson Med 54:443–448. CrossRef Medline

Schafer JR, Kida I, Xu F, Rothman DL, Hyder F (2006) Reproducibility of odor maps by fMRI in rodents. Neuroimage 31:1238–1246. CrossRef Medline

Shipley MT, Ennis M (1996) Functional organization of olfactory system. J Neurobiol 30:123–176. CrossRef Medline

Sobel N, Prabhakaran V, Desmond JE, Glover GH, Goode RL, Sullivan EV, Gabrieli JD (1998a) Sniffing and smelling: separate subsystems in the human olfactory cortex. Nature 392:282–286. CrossRef Medline

Sobel N, Prabhakaran V, Hartley CA, Desmond JE, Zhao Z, Glover GH, Gabrieli JD, Sullivan EV (1998b) Odorant-induced and sniff-induced activation in the cerebellum of the human. J Neurosci 18:8990–9001. Medline

Soucy ER, Albeanu DF, Fantana AL, Murthy VN, Meister M (2009) Precision and diversity in an odor map on the olfactory bulb. Nat Neurosci 12:210–220. CrossRef Medline

Spors H, Grinvald A (2002) Spatio-temporal dynamics of odor representations in the mammalian olfactory bulb. Neuron 34:301–315. CrossRef Medline

Strohl KP, Thomas AJ, St Jean P, Schlenker EH, Koletsky RJ, Schork NJ (1997) Ventilation and metabolism among rat strains. J Appl Physiol 82:317–323. CrossRef Medline

Tang YY, Ma Y, Fan Y, Feng H, Wang J, Feng S, Lu Q, Hu B, Lin Y, Li J, Zhang Y, Wang Y, Zhou L, Fan M (2009) Central and autonomic nervous system interaction is altered by short-term meditation. Proc Natl Acad Sci U S A 106:8865–8870. CrossRef Medline

Uchida N, Takahashi YK, Tanifuji M, Mori K (2000) Odor maps in the mammalian olfactory bulb: domain organization and odorant structural features. Nat Neurosci 3:1035–1043. CrossRef Medline

Ueki S, Domino EF (1961) Some evidence for a mechanical receptor in olfactory function. J Neurophysiol 24:12–25. Medline

Vassar R, Chao SK, Sitcheran R, Nuñez JM, Vosshall LB, Axel R (1994) Topographic organization of sensory projections to the olfactory bulb. Cell 79:981–991. CrossRef Medline

Wachowiak M, Cohen LB (2001) Representation of odorants by receptor neuron input to the mouse olfactory bulb. Neuron 32:723–735. CrossRef Medline

Wachowiak M, Shipley MT (2006) Coding and synaptic processing of sensory information in the glomerular layer of the olfactory bulb. Semin Cell Dev Biol 17:411–423. CrossRef Medline

Wilson DA, Sullivan RM (1995) The D2 antagonist spiperone mimics the effects of olfactory deprivation on mitral/tufted cell odor response patterns. J Neurosci 15:5574–5581. Medline

Xu F (2001) That's your left foot and…. Trends Neurosci 24:549–550. CrossRef Medline

Xu F, Greer CA, Shepherd GM (2000a) Odor maps in the olfactory bulb. J Comp Neurol 422:489–495. CrossRef Medline

Xu F, Kida I, Hyder F, Shulman RG (2000b) Assessment and discrimination of odor stimuli in rat olfactory bulb by dynamic functional MRI. Proc Natl Acad Sci U S A 97:10601–10606. CrossRef Medline

Xu F, Liu N, Kida I, Rothman DL, Hyder F, Shepherd GM (2003) Odor maps of aldehydes and esters revealed by functional MRI in the glomerular layer of the mouse olfactory bulb. Proc Natl Acad Sci U S A 100:11029–11034. CrossRef Medline

Xu F, Schaefer M, Kida I, Schafer J, Liu N, Rothman DL, Hyder F, Restrepo D, Shepherd GM (2005) Simultaneous activation of mouse main and accessory olfactory bulbs by odors or pheromones. J Comp Neurol 489:491–500. CrossRef Medline

Zelano C, Jiang H, Zhou G, Arora N, Schuele S, Rosenow J, Gottfried JA (2016) Nasal respiration entrains human limbic oscillations and modulates cognitive function. J Neurosci 36:12448–12467. CrossRef Medline

Zhang X, Zhang X, Firestein S (2007) Comparative genomics of odorant and pheromone receptor genes in rodents. Genomics 89:441–450. CrossRef Medline

Zhao F, Holahan MA, Houghton AK, Hargreaves R, Evelhoch JL, Winkelmann CT, Williams DS (2015) Functional imaging of olfaction by CBV fMRI in monkeys: insight into the role of olfactory bulb in habituation. Neuroimage 106:364–372. CrossRef Medline

Zhao H, Ivic L, Otaki JM, Hashimoto M, Mikoshiba K, Firestein S (1998) Functional expression of a mammalian odorant receptor. Science 279:237–242. CrossRef Medline

Zou DJ, Feinstein P, Rivers AL, Mathews GA, Kim A, Greer CA, Mombaerts P, Firestein S (2004) Postnatal refinement of peripheral olfactory projections. Science 304:1976–1979. CrossRef Medline